Photoelectron energy spectra from elastic rescattering in ultrastrong laser fields: A relativistic extension of the three-step model

S. S. Luo, P. D. Grugan, and B. C. Walker*

Department of Physics and Astronomy, University of Delaware, Newark, Delaware 19716, USA

(Received 1 November 2014; revised manuscript received 29 January 2015; published 26 March 2015)

Using a relativistic adaptation of a three-step recollision model we calculate photoelectron energy spectra for ionization with elastic scattering in ultrastrong laser fields up to 24 a.u. (2×10^{19} W/cm^2). Hydrogenlike and noble gas species with Hartree-Fock scattering potentials show a reduction in elastic rescattering beyond 6×10^{16} W/cm^2 when the laser Lorentz deflection of the photoelectron exceeds its wave-function spread. A relativistic rescattering enhancement occurs at 2×10^{18} W/cm^2, commensurate with the relativistic motion of a classical electron in a single field cycle. The noble gas results are compared with available experiments. The theory approach is well suited to modeling scattering in the ultrastrong intensity regime that lies between traditional strong fields and extreme relativistic interactions.

DOI: 10.1103/PhysRevA.91.033412 PACS number(s): 32.80.Fb, 32.80.Rm, 33.80.Rv, 33.20.Xx

I. INTRODUCTION

High strength laser fields can ionize the outer, least tightly bound electron from atoms and molecules by overcoming the binding nuclear Coulomb field. Fields of this strength (0.17 a.u., intensities of 10^{15} W/cm^2) also dominate photoelectron dynamics and the oscillating laser field can force the photoelectron to return and "rescatter" with the parent ion [1]. Over the past twenty years, strong field ionization and rescattering has been used to measure electron dynamics [2], collisionally excite multiple electrons [3], generate coherent attosecond x-ray light [4], and perform molecular tomography [5]. For optical frequency lasers, these phenomena occur on energy scales (e.g., the ponderomotive [1] or "quiver" energy $U_p = e^2|E|^2/(4m\omega^2)$ for an electron charge $-e$ in an oscillating electric field E, frequency ω) that are less than 1% of the electron rest mass m. Hence, the interaction is safely described nonrelativistically using the dipole approximation $\vec{E} \cdot \vec{r}$ in the length gauge. Models for these interactions [6–11] range from fully quantum one-electron [12] or multielectron treatments [13] to insightful one-electron [14] and multielectron classical theories [15,16].

When the laser field is increased, more tightly bound electrons ionize; up to 26 electrons have been ionized for 24 a.u. laser fields (2×10^{19} W/cm^2) [17]. In these ultrastrong fields, relativistic dynamics [18] are important and photoelectron energies can exceed several times the electron rest mass [19]. The laser field may no longer be simply approximated and the laser magnetic field B is required [20]. Research with mid-IR wavelength lasers and keV energy, attosecond XUV pulses are also beginning to venture into the ultrastrong field frontier [21]. Theoretical underpinnings common to strong field models fail in ultrastrong fields. New approaches are required to overcome the numerous challenges such as three-dimensional spatial dynamics that extend relativistically from an atomic unit of length to that of an optical wavelength in a femtosecond. Theory treatments have ranged from one-electron time-dependent Dirac and Klein-Gordon solutions [22] to fully classical [23–26]. Recent calculations have addressed the fundamental physics including the role of electron spin [27]. At this time, the theoretical approaches have reached a point where it is possible to compare with experimental results in a quantitative way. Such comparisons will make it possible to identify complex dynamics and multielectron physics.

II. RELATIVISTIC, THREE-STEP RECOLLISION MODEL

An emerging technique which accurately captures much of the physics and can be useful when comparing to experimental results involves treating interactions such as ionization [10] or radiation [28] quantum mechanically and propagation of the photoelectron in the field classically when the electron de-Broglie wavelength is much smaller than the drive wavelength. Ionization and propagation components of this model compare favorably with recent ultrastrong field experiments [17]. Monte Carlo trajectory ensembles in the model capture essential quantum aspects of the electron [23,24] and such semiclassical approaches have been compared to full quantum solutions with the Dirac equation [29]. Adding elastic rescattering is a natural extension of the model and the approach has advantages in its connection to the well-known three-step model [30]. Perhaps more important is the ability to include temporal and spatial integrated experimental conditions. Relativistic dynamics and a focal geometry inherent to all ultrastrong field experiments lead to complicated field accelerations that depend on the position and time in the laser field. Rendering a result for comparison to experimental result has involved, for example [17], integration over 10^{-3}-m distances and 10^{-13} s. There is also a natural extension of the technique to plasma physics in ultrastrong fields, which utilizes classical particle-in-cell methods.

We report photoionization and fully relativistic elastic scattering [31] in ultrastrong fields. Key questions addressed include the final photoelectron energies as they are affected by elastic rescattering [32], atomic scattering potentials, the laser magnetic field, and relativistic effects. The work helps quantify the changes in rescattering as one moves from the strong field to ultrastrong field. After the ionization process itself, elastic scattering is the primary mechanism by which

*bcwalker@udel.edu

the field energy is transferred to atomic and ion systems. Using hydrogenlike and screened atomic scattering potentials for noble gas species, we are able to model elastic rescattering as a function of intensity. Magnetic deflection effects [20] are observed beyond 6×10^{16} W/cm^2 when the rescattering parameter [33] [$\Gamma_r = U_p^{3/2} V_{IP}^{1/2}/(3c^2\omega)$ for ionization from a binding energy V_{IP}] indicates that the Lorentz deflection of the photoelectron equals its wave function spread. Relativistic scattering enhancements are observed for intensities beyond 2×10^{18} W/cm^2 where the classical field nonlinearity parameter [$a_0 = e|E|/(\omega mc)$] signifies that the electron motion is relativistic within a single field cycle. The extreme relativistic regime ($a_0 > 10$) [18] lies beyond the scope of this work. Lasers that promise to achieve extreme relativistic intensities [34] are under construction. Atomic units are used throughout the work except as noted where conventional units (e.g., W/cm^2) are used for comparison to other work.

A. Ionization

Our calculations use linearly polarized light, $\vec{E} = E_0 \sin(kz - \omega t)\exp[-(t - z/c)^2/\sigma^2]\,\hat{x}$, with a pulse duration $\sigma = 34$ fs and carrier wavelength $\lambda = 2\pi/k = 800$ nm. When considering the full field $\vec{B} = |E|/c\,\hat{y}$. In the dipole approximation we set $\vec{B} = 0$. This plane wave is used for all cases except as noted for comparison with data at 10^{19} W/cm^2 where we adopt the experimental focus. Ionization is calculated using the Ammosov-Delone-Krainov (ADK) rate [35] for hydrogenlike $1s$ states and the least tightly bound electron for the noble gas ions. The ionization curves for He^+ and Ar^{8+} are shown in Fig. 1 along with the laser electric field. To keep the comparisons across species similar, E_0 is chosen so that ionization reaches 90% by the end of the pulse. Such a treatment of the ionization rate is believed to be accurate within a factor of 2. Relativistic and Coulomb factors [36] lead to corrections in the rate of less than 25% for the cases presented here.

B. Continuum dynamics

After ionization, a Gaussian Monte Carlo ensemble electron "wave packet" is launched in the continuum with a quantum spread from the initial ionization width [33] and subsequent propagation. The deflection due to B is calculated using the Lorentz force on the photoelectron, $\vec{F} = -e\vec{E} - e\vec{v} \times \vec{B}$. As the electron interacts with a soft core potential, $\frac{Ze}{\sqrt{r^2+\delta}}$, and external field, the position and momenta for the trajectories within the Monte Carlo ensembles are generated by integrating Hamilton's equations of motion:

$$\frac{dp_x}{dt} = \frac{-Ze^2 x}{(r^2+\delta)^{3/2}} - eE_x\left[1 - \frac{p_z}{\sqrt{p^2+m^2c^2}}\right], \quad (1)$$

$$\frac{dp_y}{dt} = \frac{-Ze^2 y}{(r^2+\delta)^{3/2}}, \quad (2)$$

$$\frac{dp_z}{dt} = \frac{-Ze^2 z}{(r^2+\delta)^{3/2}} - \frac{eE_x p_x}{\sqrt{p^2+m^2c^2}}, \quad (3)$$

$$\frac{dx}{dt} = \frac{p_x c}{\sqrt{p^2+m^2c^2}}, \quad (4)$$

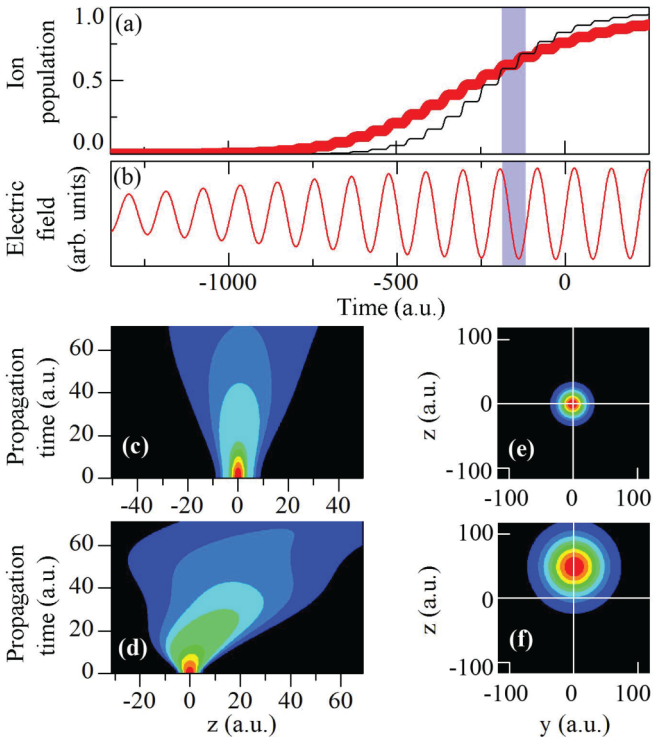

FIG. 1. (Color online) He^+ (bold) and Ar^{8+} (thin) population (a) as a function of time in the laser field (b) whose peak intensity is 2.4×10^{15} W/cm^2 for He^+ and 5.2×10^{16} for Ar^{8+}. The shaded region from -188 a.u. to -116 a.u. Panels (a) and (b) indicate the time from ionization to scattering return for (c) and (d). The continuum electron density along z during this 72-a.u. window is shown for He^+ (c) and Ar^{8+} (d). The y-z flux profile at return is shown for He^+ (e) and Ar^{8+} (f).

$$\frac{dy}{dt} = \frac{p_y c}{\sqrt{p^2+m^2c^2}}, \quad (5)$$

$$\frac{dz}{dt} = \frac{p_z c}{\sqrt{p^2+m^2c^2}}, \quad (6)$$

where c is the speed of light, δ is the soft-core parameter (typically $\delta = 0.5$), Z is the atomic number, $r = \sqrt{x^2+y^2+z^2}$, and $p = \sqrt{p_x^2+p_y^2+p_z^2}$. When only the dipole approximation is considered, the Lorentz force terms from B are zero, resulting in $p_z/\sqrt{p^2+m^2c^2}$ in Eq. (1) and E in Eq. (3) being dropped. For most calculations, the soft-core potential term is set to zero since, as we will show, it does not affect the results presented here.

Also shown in Figs. 1(c) and 1(d) is an example rescattering flux "snapshot" from a collection of electron trajectories for He^+ and Ar^{8+} with the ionization and return scattering time indicated in Figs. 1(a) and 1(b). Strong-field rescattering [Fig. 1(c)] shows the traditional spreading and return of the electron after ionization while for ultrastrong field rescattering [Fig. 1(d)] the Lorentz deflection acts to displace the electron by ~50 a.u. along z. The >20-a.u. spatial extent of the returning electron justifies a plane-wave approximation. Compared to ionization of neutrals or molecules, the plane-

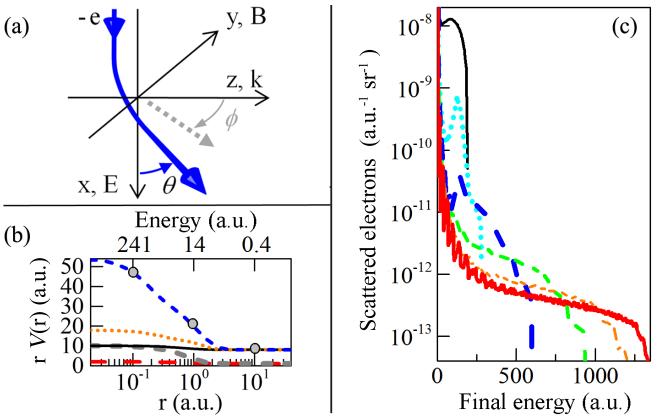

FIG. 2. (Color online) Coordinate system (a) for scattering with the parent ion (origin). The scattering potentials [plotted as effective charge in atomic units $rV(r)$ as a function of r] are shown in (b) for Xe^{8+} (dash, blue), Ar^{8+} (dotted, orange), Ne^{8+} (solid, black), Ne^{+} (thick dash, gray), and He^{+} (long dash, red). For Xe^{8+} the energy corresponding to the minimum r and effective charge for $\theta = \pi/2$ scattering is indicated by the top axis and on the Xe^{8+} potential curve (circle, filled gray). Energy and angle (θ) resolved scattering (c) from hydrogenlike ($Z = 3$) at 6×10^{16} W/cm^2 for $0.05 < \theta < 0.5$ (solid black), $0.5 < \theta < 1.0$ (dotted, light blue), $1.0 < \theta < 1.55$ (long dash, blue), $1.55 < \theta < 2.1$ (dash, green), $2.1 < \theta < 2.6$ (short dash, orange), and $2.6 < \theta < 3.14$ (thick solid, red).

wave approximation becomes more accurate for ionization in ultrastrong fields. The smaller extent of more tightly bound states results in a greater spreading of the ionized electron due to the uncertainty principle. This increase in spreading is evident when comparing the ionization of Ar^{8+} in Fig. 1(f) to that of He^{+} in Fig. 1(c). With regard to the use of trajectory ensembles in the continuum, the de Broglie wavelength of the continuum electron is typically 0.5 to 0.01 atomic units of length.

C. Elastic rescattering

Upon revisiting the parent ion, elastic scattering is calculated using a full partial-wave calculation [37]. Elastic scattering (Fig. 2) is calculated for hydrogenlike species using a bare nucleus, Coulomb potential, $V(r) = Ze/r$. Low-energy scattering with unphysically large impact parameters (given the finite extent of the electron) is avoided by eliminating scattering energies below $0.3U_p$. Neglecting these energies does not affect final-state results above $0.3U_p$. For noble gases, we use Hartree-Fock screening of the nucleus with a screening charge density given by $\rho_e(r) = \frac{Ze}{4\pi r}\sum_{i=1}^{3} D_i d_i^2 \exp^{-d_i r}$, with the D_i and d_i coefficients calculated using the ELSEPA routine [37]. The charge distribution ρ_e is used to obtain the screening potential from which scattering is calculated. While the scattering charge for hydrogenlike species is independent of r, atomic species have an effective charge that depends on the distance from the nucleus due to screening. The effective charge for scattering with Xe^{8+} is 8 for relatively large $r = 4$ a.u., increasing to 20 for an interaction at $r = 1$ a.u., and to 47 (nearly the full value of the bare nucleus) at $r = 0.1$ a.u. For $\theta = \pi/2$ scattering, the incident energies corresponding to these impact parameter distances are shown in the Fig. 2(b) top x axis. Impact parameter distances of $r = 1$ a.u. have an incident energy of 14 a.u. for $\theta = \pi/2$ scattering. At the intensity where Xe^{8+} ionization is 90%, the maximum $3.2\ U_p$ return energies of 116 hartree probe deep into the Xe^{8+} screened potential experiencing effective charges in the range $rV(r) \approx 30$. The screening potentials used for Ne^{+}, He^{+}, Ar^{8+}, and Ne^{8+} are shown in Fig. 2(d). As is well known, potentials are most accurately known for neutrals and single charge ions where experimental measurements have been done. The Ne^{8+}, Ar^{8+}, and Xe^{8+} ion potentials shown in Figs. 2(b) and 2(d) are sufficiently accurate for this work. Scattering is calculated for all ϕ and for θ between 0.05 to π radian forward to backscattering, respectively. An example of the angle and energy resolved scattering is shown in Fig. 2(c). The angle and energy integrated result from Fig. 2(c) is the total elastic scattering, which expressed as a ratio of the scattering to ionization is 2×10^{-4} for the example in Fig. 2(c).

III. RESULTS

A. Total elastic scattering

To determine the intensity dependence for angle and energy integrated scattering, we calculated the total elastic scattering for multiple species from 10^{15} to 10^{19} W/cm^2. Let us first direct attention to hydrogenlike species. These are the simplest to interpret as a function of intensity I, since a single parameter (Z) is changed as ionization proceeds from $Z = 2$ at 1.4×10^{16} W/cm^2 to $Z = 7$ at 1.6×10^{19} W/cm^2. Three different calculations are shown for the ionization, first is the nonrelativistic case where the laser field is treated in the dipole approximation ($B = 0$). The calculated electron scattering as a fraction of the total ionization at the end of the laser pulse decreases from 10^{-2} in a 10^{15} W/cm^2 strong field to 10^{-11} in the ultrastrong field at 10^{19} W/cm^2. This tremendous reduction in the rescattering efficiency is consistent with the energy scaling in Rutherford scattering. A I^{-2} fit shown in Fig. 3 is in excellent agreement with the nonrelativistic $B = 0$ case, due to a nonrelativistic recollision energy U_p that is linear in intensity. Second, we calculated the rescattering including relativistic effects in the continuum dynamics while maintaining the dipole approximation, i.e., $B = 0$. The results are similar to the nonrelativistic calculations but there is an increase by a factor of 3 at 2×10^{19} W/cm^2 due to the relativistic mass shift limiting the excursion. The onset of the relativistic enhancement effects coincide with a classical field nonlinearity parameter $a_0 > 1$. Finally we included the full interaction with relativity and B. The results follow closely the nonrelativistic and relativistic cases until 6×10^{16} W/cm^2 where scattering begins to drop. By 2×10^{17} W/cm^2 the scattering is an order of magnitude smaller than the $1/I^2$ scaling. When the intensity reaches the value of $a_0 = 1$ at 2×10^{18} W/cm^2 the yield is reduced by seven orders of magnitude. This reduction in the scattering is due to the Lorentz deflection (Fig. 1) from B [20,38] and consistent with the relativistic rescattering parameter, $\Gamma_r > 1$. The regime where Γ_r is much less than 1 may be considered in the nonrelativistic, $B = 0$ limit.

Included in Fig. 3 is scattering for noble gas ions with relativity and B. For clarity, these data points are labeled in the graph. As is indicated in Fig. 2(b), a screened potential

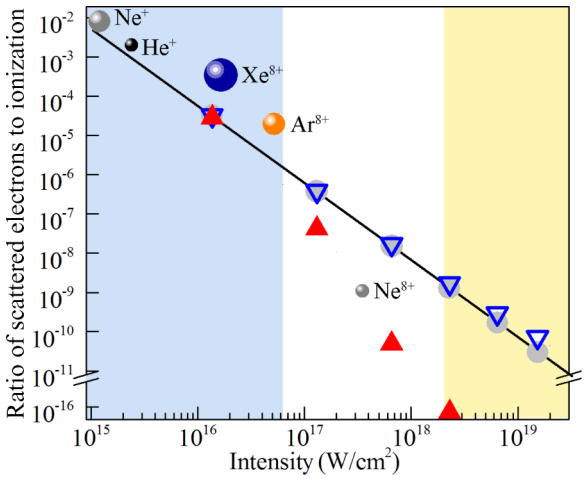

FIG. 3. (Color online) Ratio of total scattered photoionization (all angles, energies greater than $0.3U_p$) to photoionization as a function of intensity for hydrogenlike species with a nonrelativistic dipole response with $2 \leqslant Z \leqslant 7$ (circle, gray), relativistic dipole response with $2 \leqslant Z \leqslant 7$ (inverted triangle, blue), and relativistic full E, B field response with $2 \leqslant Z \leqslant 5$ (filled triangle, red). A $1/I^2$ line (solid, black) is added. Noble gas scattering (sphere) is shown for Ne^+ (gray), He^+ (small, black), Xe^{8+} (large, blue), Ar^{8+} (orange), and Ne^{8+} (small, gray). Two regions are highlighted for $\Gamma_r < 1$ (light blue) and $a_0 > 1$ (light orange).

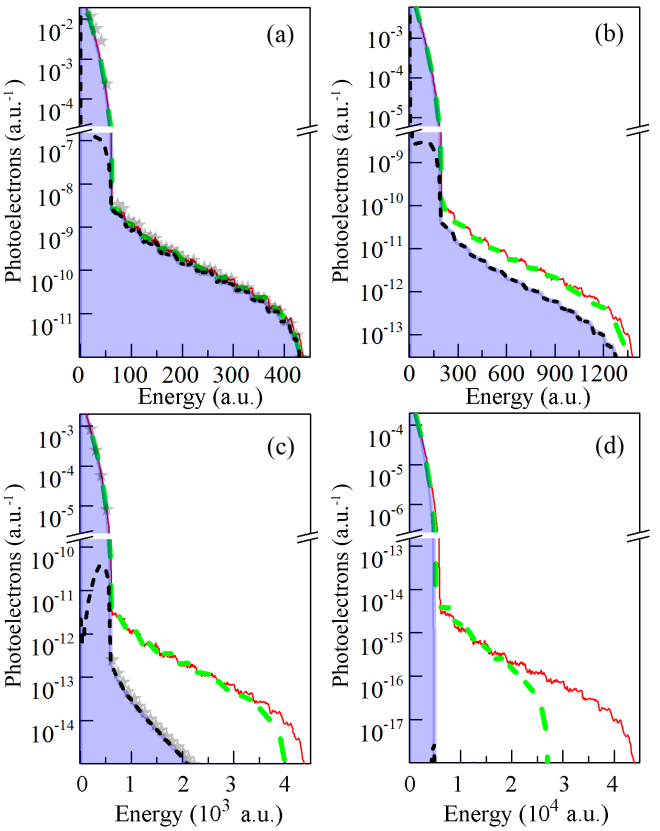

FIG. 4. (Color online) Photoelectron energy spectrum for hydrogenlike species with a nonrelativistic dipole response (thin, red), relativistic dipole response (dash, green), and relativity with B (filled, blue) at 2×10^{16} W/cm^2 (a), 6.3×10^{16} W/cm^2 (b), 2×10^{17} W/cm^2 (c), and 2×10^{18} W/cm^2 (d). The scattering component is shown (dotted, dark blue). To aid in (a)–(d) comparison the energy scale is $0 - 10.5U_p$. The results when including Coulomb focusing (gray star symbol) for the full field, relativistic calculation are shown in (a) and (c).

gives greater scattering. With scattering scaling as Z^2, the yield from an atom such as xenon can be significantly greater than a bare nucleus of the same ion charge. We begin with traditional strong field ionization of the first charge state for Ne^+ (1×10^{15} W/cm^2, $U_p = 2.2$ a.u.) and He^+ (2×10^{15} W/cm^2, $U_p = 4.4$ a.u.). The calculated total scattering is within a factor of 2 times the hydrogenlike result for the Ne^+ scattering, due to the low scattering energy. The calculated scattering for He^+ is near the hydrogenlike results as well, due in addition to the small nuclear charge of 2. Next we examine the scattering from Xe^{8+} (2×10^{16} W/cm^2) and Ar^{8+} (5×10^{16} W/cm^2). The scattering yield for Xe^{8+} and Ar^{8+} is an order of magnitude larger than the simple hydrogenlike, Coulomb ion result due to the large screened nuclear charge. Both are at $\Gamma_r < 1$ intensities. Last is an excellent test case for scattering in ultrastrong fields. Ne^{8+} at 3×10^{17} W/cm^2 has photoelectron energies on the order of $U_p = 660$ a.u. With $\Gamma_r = 15.6$, the rescattering is expected to be strongly affected by B. Looking to Fig. 3 we can see the amount of scattering for Ne^{8+} is 60 times smaller than the nonrelativistic $B = 0$ hydrogenlike case and greater than the expected relativistic hydrogenlike case with B. A result consistent with a reduction from the Lorentz deflection and slight enhancement from a screened nuclear charge of 10. Experiments are underway to verify the drastic reduction in rescattering by nine orders of magnitude over an intensity change of only a factor of 6.

B. Photoelectron energy spectra

Elastically scattered electrons are critical to understanding photoelectron final states. The maximum energy without scattering is $2U_p$ while with scattering energies [39] can reach $10U_p$. We begin the analysis of the photoelectron final energies for the three cases used previously: a traditional nonrelativistic strong-field analysis with $B = 0$, including relativistic effects while setting $B = 0$, and the full field with relativistic dynamics. We begin in Fig. 4 with hydrogenlike ions and the portion of the spectrum resulting from elastic scattering with the parent ion at 2×10^{16} W/cm^2 ($\Gamma_r = 0.14, a_0 = 0.1$), 6×10^{16} W/cm^2 ($\Gamma_r = 0.94, a_0 = 0.17$), 2×10^{17} W/cm^2 ($\Gamma_r = 6.54, a_0 = 0.31$), and 2×10^{18} W/cm^2 ($\Gamma_r = 311$, $a_0 = 0.97$).

As we progress from Fig. 4(a) to Fig. 4(d) we see the evolution of the spectra and the impact of relativity and the Lorentz deflection. The agreement between all cases [Fig. 4(a)] is consistent with a nonrelativistic, dipole interaction. With increasing intensity, the overall decrease in the contribution of elastic scattering to the photoelectron final-state energy spectrum is quantified in Fig. 4(b) for a $\Gamma_r = 0.94$ where scattering is beginning to be suppressed as B deflects the returning electron. By the intensity of 2×10^{17} W/cm^2, $\Gamma_r = 6.54$ in Fig. 4(c) nearly all elastic scattering has been suppressed with the highest energy photoelectrons most strongly affected. Finally, at $a_0 = 1$ in Fig. 4(d) one may infer

that elastic scattering in the ultrastrong field does not occur, or at least is not observable at the level of 10^{-18} electrons per hartree and steradian. For the sake of completeness we also show the spectra without the Lorentz deflection but including the relativistic mass shift. The effect of relativistic continuum dynamics is to decrease the maximum kinetic energies attained from the field and elastic scattering.

Where the excursion of the electron is comparable to the ion potential, the force from the ion can affect the photoelectron in the continuum in a process known as Coulomb focusing [40]. One might at first suppose the large parent ion charges in ultrastrong fields could lead to strong Coulomb focusing effects. However, due to the large excursion that places the photoelectron far away from the parent ion and the high momentum gained from acceleration in the external field, Coulomb focusing plays a smaller role in ultrastrong fields. The results of Figs. 4(a) and 4(c) have included the Coulomb focusing with the soft-core potential described in Eqs. (1)–(3). The increase in the rescattering can be seen in Fig. 4 but is only a fraction of the displayed symbol size.

Our last calculation is for noble gases, relativistically with full E, B fields and the scattering potentials described in Fig. 2. This work is intended to help bridge the gap between theoretical work and experimental efforts to quantify new ultrastrong field physics. To begin we connect to earlier, nonrelativistic strong-field observations. Experimental data [39] is plotted in Fig. 5(a) along with our results for Ne^+. Our calculations are consistent with the well-known strong-field response and previous results [39]. In Fig. 5(b) the photoelectron energy spectrum for Ar^{8+} is shown. With a $\Gamma_r = 0.87$, Ar^{8+} is beginning to be effected by B. The scattering reduction seen in Fig. 5(b) is consistent with the Lorentz rescattering parameter factor of $\exp(-\Gamma_r)$. In Fig. 5(c) the Ne^{8+} calculation reveals that at 3×10^{17} W/cm^2 for $\Gamma_r = 15.6$, scattering may be neglected since its occurrence is at the level of 10^{-14} electron per hartree and steradian). The highest intensity presented is 1.2×10^{19} W/cm^2 for the ionization of Xe at $\Gamma_r = 7480$, $a_0 = 2.4$. To compare with experiments, Fig. 5(d) has been modeled using the experimental focus, spatial volume, energy resolution, angular acceptance [17,41], and multiple charge state distribution expected as ionization proceeds from neutral Xe to Xe^{26+} by the end of the pulse. Comparing the data with our calculation, one can see that the high-energy rescattering expected nonrelativistically is absent.

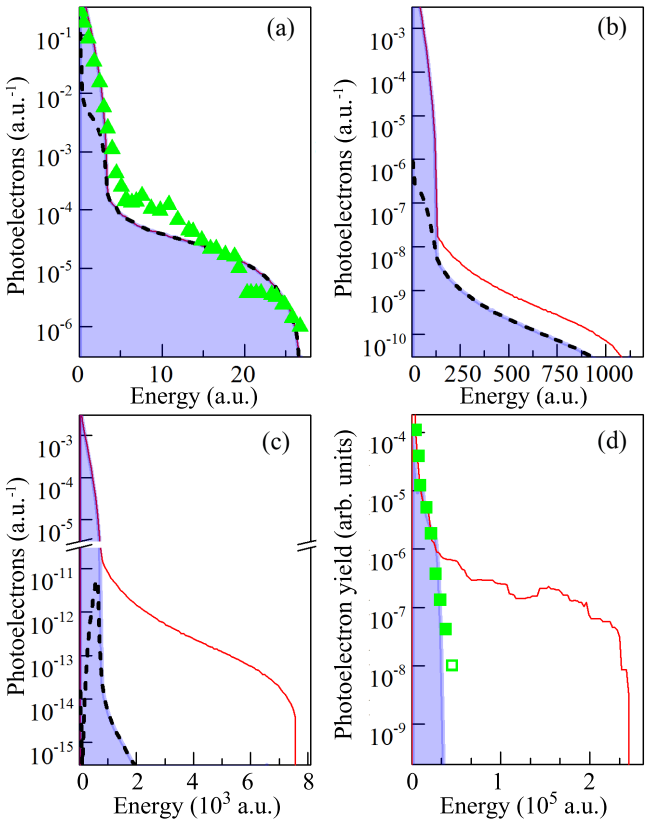

FIG. 5. (Color online) Energy resolved photoelectron spectrum for Ne^+ (a), Ar^{8+} (b), Ne^{8+} (c), Xe^+ to Xe^{26+} (d), and a nonrelativistic dipole (thin, red), relativistic, E, B response (filled, blue) with the partial yield from rescattering (dotted, dark blue). Experimental data is shown (triangle) [39] and (square) [41]. For (d) the nonrelativistic response (thin, red) has been multiplied by 120 from the calculated value (dotted, red) to compare with the data. The open square data point in (d) is the limit of the signal to noise for that experimental energy.

IV. CONCLUSION

A three-step model is extended into the relativistic, ultrastrong field regime ($\Gamma_r > 1$ and $a_0 < 10$). Continuum dynamics are treated semiclassically with Monte Carlo trajectory ensembles to account for relativistic and B effects while ionization and rescattering is treated quantum mechanically. Studies of scattering in hydrogenlike systems show elastic rescattering generally obeys a $1/I^2$ scaling when the Lorentz deflection is small, i.e., $\Gamma_r < 1$. Elastic scattering decreases roughly as a function of $\exp(-\Gamma_r)$ until becoming undetectable. Relativistic mass effects are noted but play a smaller role, contributing for intensities beyond 10^{18} W/cm^2. In addition to work with fundamental hydrogenlike species, we calculated how the elastic scattering would be observed for noble gas species with screened atomic potentials. The results compare favorably with experimental data.

ACKNOWLEDGMENTS

This material was based upon work supported by the Army Research Office under Award No. W911NF-09-1-0390 and the National Science Foundation under Award No. PHY-1307042.

[1] L. F. DiMauro and P. Agostini, Adv. At. Mol. Opt. Phys. D **35**, 79 (1995).

[2] Y. Huismans, A. Rouzee, A. Gijsbertsen, J. H. Jungmann, A. S. Smolkowska, P. S. W. M. Logman, F. Lepine, C. Cauchy, S. Zamith, T. Marchenko, J. M. Bakker, G. Berden, B. Redlich, A. F. G. van der Meer, H. G. Muller, W. Vermin, K. J. Schafer, M. Spanner, M. Y. Ivanov, O. Smirnova, D. Bauer, S. V. Popruzhenko, and M. J. J. Vrakking, Science **331**, 61 (2011).

[3] T. Weber, H. Giessen, M. Weckenbrock, G. Urbasch, A. Staudte, L. Spielberger, O. Jagutzki, V. Mergel, M. Vollmer, and R. Dorner, Nature (London) **405**, 658 (2000).
[4] M.-C. Chen, C. Mancuso, C. Hernandez-Garcia, F. Dollar, B. Galloway, D. Popmintchev, P.-C. Huang, B. Walker, L. Plaja, A. A. Jaron-Becker, A. Becker, M. M. Murnane, H. C. Kapteyn, and T. Popmintchev, Proc. Natl. Acad. Sci. U.S.A. **111**, E2361 (2014).
[5] J. Itatani, J. Levesque, D. Zeidler, H. Niikura, H. Pepin, J. Kieffer, P. Corkum, and D. Villeneuve, Nature (London) **432**, 867 (2004).
[6] D. B. Milosevic, G. G. Paulus, D. Bauer, and W. Becker, J. Phys. B: At., Mol. Opt. Phys. **39**, R203 (2006).
[7] A. LHuillier, K. Schafer, and K. Kulander, J. Phys. B: At., Mol. Opt. Phys. **24**, 3315 (1991).
[8] K. Burnett, V. Reed, and P. Knight, J. Phys. B: At., Mol. Opt. Phys. **26**, 561 (1993).
[9] A. Becker and F. Faisal, J. Phys. B: At., Mol. Opt. Phys. **38**, R1 (2005).
[10] V. Popov, Phys. Usp. **47**, 855 (2004).
[11] P. Lambropoulos, P. Maragakis, and J. Zhang, Phys. Rep. Phys. Lett. **305**, 203 (1998).
[12] H. van der Hart, B. Doherty, J. Parker, and K. Taylor, J. Phys. B: At., Mol. Opt. Phys. **38**, L207 (2005).
[13] J. Parker, L. Moore, D. Dundas, and K. Taylor, J. Phys. B: At., Mol. Opt. Phys. **33**, L691 (2000).
[14] A. Kamor, C. Chandre, T. Uzer, and F. Mauger, Phys. Rev. Lett. **112**, 133003 (2014).
[15] W. Liu, J. Eberly, S. Haan, and R. Grobe, Phys. Rev. Lett. **83**, 520 (1999).
[16] P. Ho, R. Panfili, S. Haan, and J. Eberly, Phys. Rev. Lett. **94**, 093002 (2005).
[17] N. Ekanayake, S. Luo, P. D. Grugan, W. B. Crosby, A. D. Camilo, C. V. McCowan, R. Scalzi, A. Tramontozzi, L. E. Howard, S. J. Wells, C. Mancuso, T. Stanev, M. F. Decamp, and B. C. Walker, Phys. Rev. Lett. **110**, 203003 (2013).
[18] A. Di Piazza, C. Mueller, K. Z. Hatsagortsyan, and C. H. Keitel, Rev. Mod. Phys. **84**, 1177 (2012).
[19] A. D. DiChiara, I. Ghebregziabher, R. Sauer, J. Waesche, S. Palaniyappan, B. L. Wen, and B. C. Walker, Phys. Rev. Lett. **101**, 173002 (2008).
[20] M. Walser, C. Keitel, A. Scrinzi, and T. Brabec, Phys. Rev. Lett. **85**, 5082 (2000).
[21] M. Chini, K. Zhao, and Z. Chang, Nat. Photon. **8**, 178 (2014).
[22] H. Bauke, H. G. Hetzheim, G. R. Mocken, M. Ruf, and C. H. Keitel, Phys. Rev. A **83**, 063414 (2011).
[23] S. S. Luo, P. D. Grugan, and B. C. Walker, J. Phys. B: At., Mol. Opt. Phys. **47**, 135601 (2014).
[24] P. D. Grugan, S. Luo, M. Videtto, C. Mancuso, and B. C. Walker, Phys. Rev. A **85**, 053407 (2012).
[25] S. X. Hu and A. F. Starace, Phys. Rev. E **73**, 066502 (2006).
[26] A. Maltsev and T. Ditmire, Phys. Rev. Lett. **90**, 053002 (2003).
[27] M. Klaiber, E. Yakaboylu, C. Müeller, H. Bauke, G. G. Paulus, and K. Z. Hatsagortsyan, J. Phys. B: At., Mol. Opt. Phys. **47**, 065603 (2014).
[28] J.-X. Li, K. Z. Hatsagortsyan, and C. H. Keitel, Phys. Rev. Lett. **113**, 044801 (2014).
[29] M. Klaiber, E. Yakaboylu, H. Bauke, K. Z. Hatsagortsyan, and C. H. Keitel, Phys. Rev. Lett. **110**, 153004 (2013).
[30] P. Corkum, Phys. Rev. Lett. **71**, 1994 (1993).
[31] A.-T. Le, R. R. Lucchese, S. Tonzani, T. Morishita, and C. D. Lin, Phys. Rev. A **80**, 013401 (2009).
[32] B. Walker, B. Sheehy, K. Kulander, and L. DiMauro, Phys. Rev. Lett. **77**, 5031 (1996).
[33] S. Palaniyappan, I. Ghebregziabher, A. DiChiara, J. MacDonald, and B. C. Walker, Phys. Rev. A **74**, 033403 (2006).
[34] G. V. Dunne, Eur. Phys. J. D **55**, 327 (2009).
[35] M. Ammosov, N. Delone, and V. Krainov, Zh. Eksp. Teor. Fiz. **91**, 2008 (1986).
[36] M. Klaiber, E. Yakaboylu, and K. Z. Hatsagortsyan, Phys. Rev. A **87**, 023417 (2013).
[37] F. Salvat, A. Jablonski, and C. Powell, Comput. Phys. Commun. **165**, 157 (2005).
[38] C. Chirila, C. Joachain, N. Kylstra, and R. Potvliege, Phys. Rev. Lett. **93**, 243603 (2004).
[39] B. Sheehy, R. Lafon, M. Widmer, B. Walker, L. F. DiMauro, P. A. Agostini, and K. C. Kulander, Phys. Rev. A **58**, 3942 (1998).
[40] D. Shafir, H. Soifer, C. Vozzi, A. S. Johnson, A. Hartung, Z. Dube, D. M. Villeneuve, P. B. Corkum, N. Dudovich, and A. Staudte, Phys. Rev. Lett. **111**, 023005 (2013).
[41] A. D. DiChiara, I. Ghebregziabher, J. M. Waesche, T. Stanev, N. Ekanayake, L. R. Barclay, S. J. Wells, A. Watts, M. Videtto, C. A. Mancuso, and B. C. Walker, Phys. Rev. A **81**, 043417 (2010).